Induction Heating Adaptation of a Different Sized Load with Matching Secondary Inductor to Achieve Uniform Heating and Enhance Vertical Displacement

Emilio Plumed, *Student Member, IEEE,* Ignacio Lope, *Member, IEEE,* and Jesús Acero, *Senior Member, IEEE*

***Abstract*—This paper presents an Inductively Coupled Heating application, that is, a combination of Wireless Power Transfer and Induction Heating. The addition of a secondary inductor with resonant capacitor directly beneath and attached to the ferromagnetic load allows to improve Induction Heating adaptation of loads of different sizes to the primary inductor, enhancing power distribution and extending load distance while avoiding increased power losses and stress on electronic components. The extended distance can be used to implement the seamless induction concept, where the typical ceramic glass is substituted by the kitchen surface itself. Finite Element Analysis simulations are carried out to determine the suitability of each possible design, and a scoring system is applied to determine the optimal solution, bearing in mind the delivered power, power factor, power distribution and efficiency. A near optimal design is chosen to develop as a prototype. The prototype is tested under working conditions up to 3680 W at several distances, validating the simulations' impedance parameters and verifying power distribution with a water boiling test and a dry test with a thermographic camera.**

***Index Terms*—Induction heating, wireless power transfer, electromagnetic simulation, electromagnetic coupling, home appliances.**

I. Introduction

FOR nearly 40 years now, induction heating (IH) has been an active research field with many contributions and improvements [1], [2] that have made these systems safer, faster, easier to use and more flexible [3]–[12]. Likewise, Wireless Power Transfer (WPT) has had numerous contributions in recent years [13]–[18]. More recently still, there have been some applications that combined IH and WPT where heating is the primary goal [19]–[24], which is named inductively coupled heating (ICH) in this paper.

Up to now, the concept of flexibility in induction cooktops has been defined as the capability to place any cooking vessel anywhere [25], in contrast to the fixed burners of traditional stoves. Most implementations have striven to cover the entire appliance area with inductors, either with many windings of small diameter [26]–[28] or a smaller number of bigger overlapped windings [29]. Others have studied the possibility of a small number of mobile inductors to cover the entire area via robotic arms [30], [31].

Fig. 1. Proposed system geometry with appliance and primary inductor beneath the kitchen surface and load with attached secondary inductor above.

Though feasible, most implementations that rely on a big number of inductors faced severe problems, such as:

- Inductor activation and inability to deliver the required power in a significant number of use cases due to intricate inverter to inductor paths and control, as well as impedance detection.
- Power distribution due to the unavoidable granularity of power delivery and the interactions between magnetic fields generated by small inductors close together.
- High electronics stress with very small inductors, which would be exacerbated with distance increments [12].

Mobile inductors had to face other issues, such as collision avoidance, accurate positioning, noise, and wear and tear of the moving parts.

This paper presents a narrower definition of flexibility, but hopefully no less desirable, both in terms of user preference and potential cost savings. Additionally, the proposed system can be used to easily implement the seamless induction concept, which substitutes the typical ceramic glass with the thicker kitchen surface itself, removing the need for a hole to fit the appliance and resulting in a seamless surface. Instead

Emilio Plumed and Jesús Acero are with the Department of Electronic Engineering and Communications, Universidad de Zaragoza, Zaragoza, Aragón, Spain, (e-mail: eplumed@unizar.es).

Ignacio Lope is with BSH Electrodomésticos España, Zaragoza, Aragón, Spain and the Department of Applied Physics, Universidad de Zaragoza, Zaragoza, Aragón, Spain.

This work was partly supported by the Spanish MINECO under Project PID2019-103939RB-I00, by the Spanish MICINN and AEI under Project RTC-2017-5965-6, co-funded by EU through FEDER program, by the BSH Home Appliances Group and by the Gobierno de Aragón-FSE 2014-20 under Grant IIU/2023/2017.

Manuscript received xxx xx, xxxx; revised xxx xx, xxxx.

of being able to place any vessel anywhere, the user would be able to place any compatible vessel with its attached secondary inductor, regardless of its diameter, on a number of predetermined points. The use of ICH allows to decouple the cooking appliance from the cooking vessel to some extent. An appliance with several identical primary inductors and resonant inverter topology would be able to deliver power to vessels of a particular ferromagnetic material of any size, shape and distance thanks to the use of attached secondary inductors and resonant capacitors. Each vessel would require specific secondary inductor designs, adapting its size, number of turns and resonant capacitor.

Such a change would simplify the design and construction of the appliance in order to focus the design process on the vessels themselves and their new electronics. Fig. 1 shows a possible implementation with a ∅ 180 mm primary inductor, a ∅ 290 mm secondary inductor and cooking vessel and a 20 mm thick kitchen surface instead of the conventional 4 mm ceramic glass. A ∅ 180 mm inductor is able to achieve adequate coupling with secondary inductors ranging from ∅ 90 mm to ∅ 300 mm, making its size the most versatile for the primary inductor role. It is worth remarking that the secondary inductor has to be attached to the ferromagnetic vessel and it is not part of a separate hob. The main goal of this implementation is to be able to deliver the full rated power to every load, with an even temperature distribution, without penalizing the electronics and able to function correctly in current conventional appliances and, more importantly, future implementations beneath kitchen surfaces [12], [19], where inductor to vessel gap can increase from the 4 mm of typical applications up to 40 mm, an order of magnitude higher. Unless otherwise specified, the distance considered will be the ceramic glass or kitchen surface thickness, in other words, the distance between primary and secondary inductors in a ICH system or the inductor to load distance in a IH system.

Current commercial applications of the seamless induction concept are limited because said surfaces need to be specially adapted to house the coils in order to maintain low distances. Small distances are required because inductor efficiency and load resistance decrease quickly with increased distance, a phenomenon which is aggravated in coils of smaller diameter. Moreover, the reduced material thickness in high stress zones, both mechanical and thermal, make the systems easier to fracture and break. ICH could be directly implemented into most kitchen surfaces just by attaching the primary coils to the bottom of the surface and relying on the secondary inductor-vessel combinations to offset the negative effects of increased distance and maintain the surfaces' structural integrity.

It is also important to mention that even though the proposed system is a hybridization of IH and WPT technologies, the system can be designed in such a way not to need complex topologies or complicated control methods. The system will use the most common topology and control method in IH, the half-bridge resonant inverter and frequency control.

The paper is divided as follows: Section II discusses the means to model the system and its design process. Section III provides simulation results that were used to develop the prototype. Section IV presents the prototype design and compares it to conventional IH systems. Section V introduces the experimental setup and the measurements results. Finally, Section VI sets forth the conclusions drawn from this work.

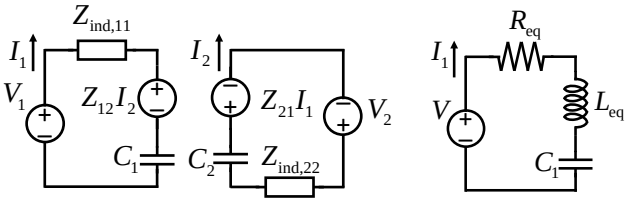

Fig. 2. Circuit diagrams of (a) full ICH system (b) equivalent system.

II. System Model and Design Guidelines

A. System Impedance

In conventional IH the inductor-load system is modelled as a frequency dependent equivalent resistance and inductance, $Z_{\text{ind},ii} = R_{ii} + j\omega L_{ii}$. In WPT the interaction between inductors is modelled as a mutual inductance, which can be put in terms of the self impedances of each inductor via the coupling coefficient, $k_{ij} = L_{ij}/\sqrt{L_{ii}L_{jj}}$. In ICH, besides having equivalent self impedances, the mutual impedance between inductors also has a resistive component due to the ferromagnetic vessel: $Z_{\text{ind},ij} = R_{ij} + j\omega L_{ij}$. Both primary and secondary inductors also have resonant capacitors to compensate the inductance. Series-series compensation was chosen in this case because it is the most advantageous in most situations [32]–[34]. The complete system can be easily modelled by the circuit shown in Fig. 2 (a) and the system of equations:

$$\begin{pmatrix} Z_{11} & Z_{12} \\ Z_{21} & Z_{22} \end{pmatrix} \begin{pmatrix} I_1 \\ I_2 \end{pmatrix} = \begin{pmatrix} V_1 \\ V_2 \end{pmatrix}, \tag{1}$$

where:

$$\begin{aligned} Z_{ii} &= Z_{\text{ind},ii} + 1/(j\omega C_i) \;\forall\; i = 1, 2, \\ Z_{ij} &= Z_{\text{ind},ij} \;\forall\; i \neq j, \end{aligned} \tag{2}$$

I_i is the current through the ith inductor and V_i is the voltage fed to the ith inductor. Given that the impedance matrix is symmetric and the secondary inductor has no external voltage, i.e. $V_2 = 0$, the system can be simplified to:

$$V/I_1 = Z_{\text{eq}} = Z_{11} - Z_{12}^2/Z_{22}. \tag{3}$$

It is useful to separate Z_{eq} into its real and imaginary components, the equivalent resistance, R_{eq}, and equivalent inductance plus resonant capacitor, L_{eq} and C_1, respectively:

$$Z_{\text{eq}} = R_{\text{eq}} + j\omega L_{\text{eq}} + 1/(j\omega C_1), \tag{4}$$

as shown also on Fig. 2 (b). The full expressions for R_{eq} and L_{eq} are:

$$R_{\text{eq}} = R_{11} + \frac{2R_{12}\omega L_{12}\left(\omega L_{22} - \frac{1}{\omega C_2}\right) - \left(R_{12}^2 - \omega^2 L_{12}^2\right) R_{22}}{R_{22}^2 + \left(\omega L_{22} - \frac{1}{\omega C_2}\right)^2}, \tag{5}$$

$$L_{\text{eq}} = L_{11} + \frac{2R_{12}\omega L_{12}R_{22} - \left(R_{12}^2 - \omega^2 L_{12}^2\right)\left(\omega L_{22} - \frac{1}{\omega C_2}\right)}{\omega\left(R_{22}^2 + \left(\omega L_{22} - \frac{1}{\omega C_2}\right)^2\right)}. \tag{6}$$

In order to obtain the terms for the impedance matrix, the geometry shown in Fig. 1 was simulated with the finite element tool Comsol Multiphysics. The simulation solves Maxwell's equations formulated with the vector magnetic potential, $\mathbf{A}$, when a known current is driven through each inductor. The induced voltage in the inductors, V_{ij}, is calculated and divided by the input current to get each impedance element:

$$Z_{\text{ind},ij} = V_{ij}/I_i, \tag{7}$$

where i denotes the inductor where the input current is driven and j denotes the inductor whose induced voltage is being calculated.

B. Design Considerations

ICH systems, as well as typical IH and WPT systems, are designed by their geometry, inductors' number of turns, inverter topology, operating frequency and resonant tank. In this case, some of the geometry is restricted because one of the design goals is to be able to use the same primary inductor for all vessel variations. The system has to function in a range of distances between inductors, d_{inds}, between 6 and 50 mm. The other input parameters in the Finite Element Analysis (FEA) simulations is the secondary's internal radius, r_{int}, and operating frequency.

In most WPT applications, the term R_{ij} is purely lossy, however, as ICH is an induction heating application, R_{ij} can be separated into:

$$R_{ij} = R_{\text{load},ij} + R_{\text{sh},ij} + R_{\text{w,cond},ij} + R_{\text{w,prox},ij}, \tag{8}$$

where $R_{\text{load},ij}$ is the load resistance, the most significant part, $R_{\text{sh},ij}$ is the aluminum shielding resistance, $R_{\text{w,cond},ij}$ is the winding's conduction losses resistance (DC + skin effect), which is zero when $i \neq j$ and $R_{\text{w,prox},ij}$ is the winding's proximity losses resistance.

For series-series resonant tanks, there can be three distinct resonant frequencies in a two inductor system: individual resonances for the primary inductor, $\omega_{\text{res},1} = 1/\sqrt{L_{11}C_1}$, and secondary inductor, $\omega_{\text{res},2} = 1/\sqrt{L_{22}C_2}$ and a resonance for the global system, $\omega_{\text{res}} = 1/\sqrt{L_{\text{eq}}C_1}$. Most inductive WPT implementations select their resonant capacitors so that $\omega_{\text{res},1} = \omega_{\text{res},2} = \omega_{\text{res}}$. This simple design rule is sound because mutual impedance in these systems is purely inductive. A resistance in the receiver gets reflected as a resistance in the transmitter, if $Z_{12} = j\omega L_{12}$, then the global impedance at secondary resonance becomes:

$$Z_{\text{eq}\,@\omega_{\text{res},2}} = R_{11} + \omega_{\text{res},2}^2 L_{12}^2/R_{22}. \tag{9}$$

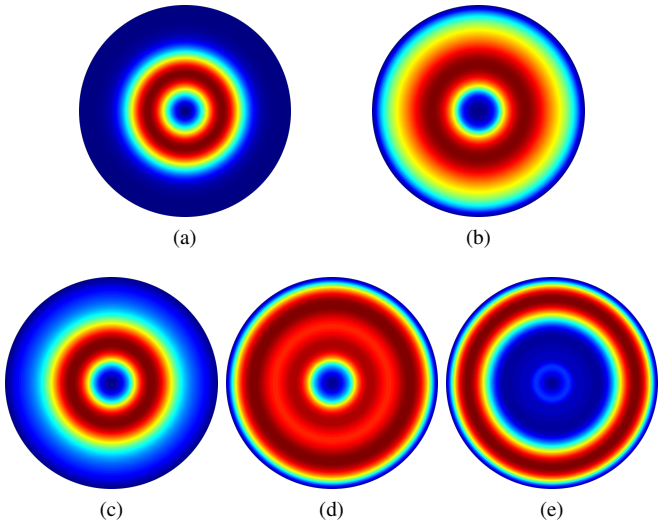

Fig. 3. Power distribution of (a) primary only, (b) secondary only, and both due to current phase differences of: (c) 0º, (d) 135º, (e) 180º.

However, if Z_{12} has a real component, i.e., $Z_{12} = R_{12} + j\omega L_{12}$, then:

$$Z_{\text{eq}\,@\omega_{\text{res},2}} = R_{11} - (R_{12}^2 - \omega_{\text{res},2}^2 L_{12}^2 + 2j\omega_{\text{res},2}R_{12}L_{12})/R_{22}. \tag{10}$$

The usual cancellation of the self inductance in both inductors causes an overcompensation in Z_{eq}, making it capacitive [22]. Therefore, in ICH, the system's resonant frequency can not be equal to the primary inductor's and secondary inductor's at the same time: $\omega_{\text{res},1} = \omega_{\text{res},2} \neq \omega_{\text{res}}$.

Current phase difference between the primary and secondary inductors is decisive for the power distribution on the vessel's surface [11]. This power distribution is calculated with Poynting's vector: $\mathbf{S} = \mathbf{E} \times \mathbf{H}^*$, where $\mathbf{E}$ is the electric field and $\mathbf{H}^*$ is the complex conjugate of the magnetic field. The total fields are a result of the sum of the fields generated by each inductor, and the fields themselves are proportional to their current phasors and their inductor's number of turns: $\mathbf{E} = n_1 I_1 \mathbf{E}_{1,\text{pt,pA}} + n_2 I_2 \mathbf{E}_{2,\text{pt,pA}}$, $\mathbf{H}^* = n_1 I_1^* \mathbf{H}_{1,\text{pt,pA}}^* + n_2 I_2^* \mathbf{H}_{2,\text{pt,pA}}^*$, where n_i is the ith inductor's number of turns, I_i is the ith inductor's current and the subscripts pt and pA mean "per turn" and "per Ampere" respectively. $\mathbf{E}_{i,\text{pt,pA}}$ and $\mathbf{H}_{i,\text{pt,pA}}$ are obtained through FEA simulations. With these expressions, $\mathbf{S}$ can be expanded to:

$$\begin{aligned}\mathbf{S} = {} & n_1^2 |I_1|^2 \mathbf{E}_{1,\text{pt,pA}} \mathbf{H}_{1,\text{pt,pA}}^* + n_1 n_2 I_1 I_2^* \mathbf{E}_{1,\text{pt,pA}} \mathbf{H}_{2,\text{pt,pA}}^* + \\ & + n_2 n_1 I_2 I_1^* \mathbf{E}_{2,\text{pt,pA}} \mathbf{H}_{1,\text{pt,pA}}^* + n_2^2 |I_2|^2 \mathbf{E}_{2,\text{pt,pA}} \mathbf{H}_{2,\text{pt,pA}}^*.\end{aligned} \tag{11}$$

The first and last terms are only affected by current amplitude and the cross terms are affected by both amplitude and phase difference. The interaction between magnetic fields generated by these cross terms can be constructive or destructive, according to the phase difference. Since one of the main goals is to obtain an even power distribution, close attention must be given to the inductor currents, both phase and amplitude, and by extension to the impedance elements that can be changed by design.

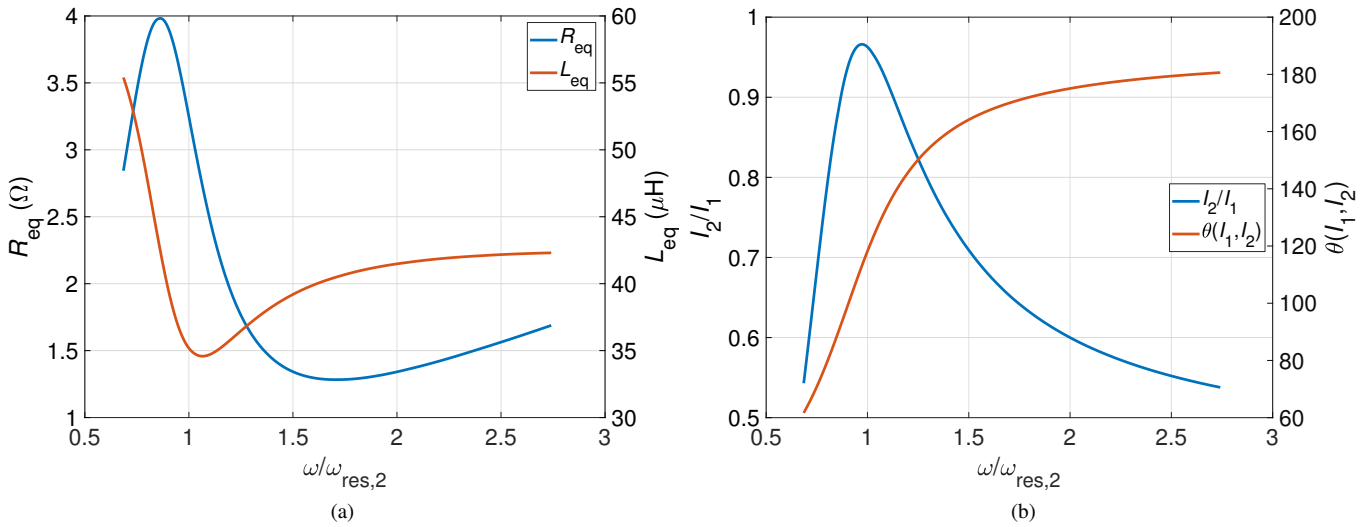

Fig. 4. Variation with relative frequency of (a) R_{eq} and L_{eq}, (b) Currents ratio and phase difference.

An example of this interaction is shown on Fig. 3, with data extracted from FEA simulations of two inductors separated 20 mm with the ∅ 290 mm load placed on top of the second one. The figure represents the power distribution of the small primary inductor in (a), the big secondary inductor in (b) and combinations of the two in (c)-(e) for different phase angles. The inductors are fed with 1 Ampere-turn in all cases, though the generated power distribution varies. Each subfigure has a different absolute maximum and its color scale is relative. When the currents are in phase, the center of the load has the most power density, while it decreases sharply at higher diameters. When they are in opposite phase, the field generated by the primary inductor is completely canceled and the highest power density is found in outer diameters. For an intermediate obtuse angle, the primary's contribution is reduced enough to have a nearly uniform power distribution across the entire surface. The optimum phase angle is entirely dependant on the magnetic field distribution, and consequently, on the system's geometry and materials, as well as the currents' amplitude.

In our proposed system, inductor currents can not be controlled independently, and the optimum phase angle has to be achieved with the design of the secondary resonant tank at a specific frequency. This limitation prevents the design process to decouple the optimal power distribution from other relevant parameters, making power distribution an important part of the optimization process.

Considering that most impedance elements are frequency dependent, namely $R_{ij}(\omega)$ and $L_{ij}(\omega)$, but said dependence can not be easily approximated, purely analytical methods are discouraged to optimize the general problem and obtain optimal design parameters. Unfortunately, the systems need to be analyzed case by case numerically, although several design rules can be gleaned from these calculations.

A great emphasis needs to be put into the secondary's resonant frequency $\omega_{res,2} = 1/\sqrt{L_{22}C_2}$, which is directly related to a maximum in equivalent resistance, R_{eq}, a minimum in equivalent inductance, L_{eq}, shown in Fig. 4 (a) and a maximum in current ratio, $|I_2|/|I_1|$ [23], shown in Fig. 4 (b). Additionally, the phase angle difference between currents increases with frequency, as shown in Fig. 4 (b), and the optimum frequency for power distribution usually obeys $\omega > \omega_{res,2}$. For example, the case depicted in Fig. 3 has its optimum phase difference near 135°.

The proximity of $\omega_{res,2}$ to global resonance, ω_{res}, also affects the phenomenon known in WPT as pole splitting [35]. Close resonant frequencies cause the R_{eq} maximum peak to be higher and thinner, giving the power curve two peaks. The closer $\omega_{res,2}$ and ω_{res} are, the greater the effect. Most WPT applications avoid the problem by working at a fixed frequency, but IH has traditionally controlled power delivery with frequency, so the design also has to minimize the pole splitting in order for ICH to function correctly with a traditional IH topology and control method.

Taking all of this into account, the design goals are to:

- Deliver power up to 3680 W (230 V × 16 A mains input) using frequency control only.
- Achieve optimal power distribution at a medium power rating and avoid bad distributions in other cases.
- Minimize system reactance in order to reduce inductor current and capacitor voltage for all power ratings, especially at high power.
- Minimize pole splitting.
- Achieve good efficiency.
- Maintain previous design goals for distances between primary and secondary inductors from 6 mm to 50 mm.

C. Score Definition

The main challenge to overcome in the design is the harmonization of several design goals that are partially opposed. The most extreme example is shown with the power factor and power distribution. The most advantageous frequencies for the power distribution are located above secondary resonance, while the most advantageous frequencies for power factor are below secondary resonance. The interaction between power reach and power factor depends on the equivalent resistance

peak. Power factor will improve with higher resistances, but since this is a voltage fed system, power will decrease.

If there were only two optimization parameters, Pareto techniques could have been used. Four, however, are very unwieldy for such methods. In order to assign a quantitative value to the compliance of each design with these goals, a score system is introduced to measure the ability to reach 3680 W, the uniformity of power distribution, the system's reactance and the efficiency.

The power reach score, PR, is defined as the ratio between the maximum power and 3680 W, with its upper value limited at 1.

The power distribution score, PD, will be the relative standard deviation of power distribution, where low values are desired:

$$PD = \sqrt{\frac{\sum_{i=1}^{N}\left(\frac{S_{z_i}}{\bar{S}_z} - 1\right)^2}{N-1}}, \tag{12}$$

where S_z is the vertical component of Poynting's vector, the index i represents the ith point of a total of N mesh points from the Finite Element Analysis (FEA) simulation that are on the bottom of the ferromagnetic load and $\bar{S}_z$ represents the mean value. For visual reference, PD for the cases presented in Fig. 3 are (a) 0.767, (b) 0.468 and (c) 1.067.

The system's reactance is measured with the electric power factor, PF, which indicates how close the system is to resonance, and therefore, the absence of reactance that increases currents and voltages unnecessarily. It can be defined as the ratio between R_{eq} and the absolute value of Z_{eq}:

$$PF = \frac{R_{\text{eq}}}{|Z_{\text{eq}}|}. \tag{13}$$

PF does not correspond to a measure of efficiency, since R_{eq} includes components of useful power and losses, and $|Z_{\text{eq}}|$ includes elements of active and reactive power. Therefore, the efficiency will be calculated as the useful power versus total power delivered to the inductive system. All power losses are modeled as resistances which are included in the impedance matrix elements (8). Total power dissipated due to each kind of resistance can be calculated from the matrix operation on the resistances from (8):

$$P = \begin{pmatrix} I_1^* & I_2^* \end{pmatrix} \begin{pmatrix} R_{11} & R_{12} \\ R_{21} & R_{22} \end{pmatrix} \begin{pmatrix} I_1 \\ I_2 \end{pmatrix}, \tag{14}$$

where the P is the power delivered by all matrix elements and the superscript * denotes the complex conjugate.

Total efficiency, η_{total}, is defined as the useful power divided by the total power delivered to the system:

$$\eta_{\text{total}} = P_{\text{load}} / \left(P_{\text{load}} + P_{\text{sh}} + P_{\text{w,cond}} + P_{\text{w,prox}}\right), \tag{15}$$

where the subscripts are the same as in (8), accounting for load power, aluminum shielding power losses, wire conduction power losses and wire proximity power losses, respectively.

Although there is no explicit score to minimize the pole splitting, the optimization with the previous scores ensures that $\omega_{\text{res},2} < \omega_{\text{res}}$, avoiding operating in the valley between power peaks.

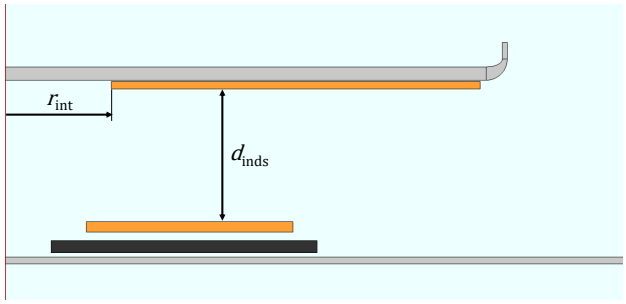

Fig. 5. Simplified 2D simulation geometry.

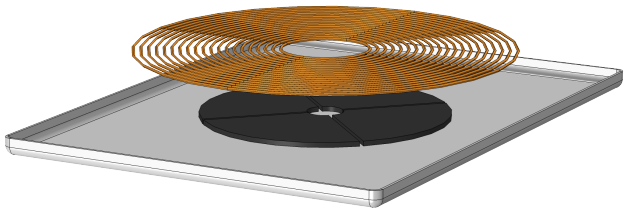

Fig. 6. Detailed elements in the 3D simulation differing from the 2D simulated system.

The impedance values obtained in the next Section will be used to design a prototype with these goals in mind, choosing values for r_{int} and C_2.

III. Simulation Results

In this section, the proposed system is modelled according to the circuit presented in the previous section. The impedance matrix is then obtained from FEA simulations. According to the degrees of freedom available, several designs are put forward and their scores defined in the previous section are calculated. Finally, a global score is defined to determine the optimal design and the results are represented.

The system presented in Fig. 1 was first simplified into a 2D model with continuous ferrite and a circular aluminum plate. The simplified geometry shown in Fig. 5 was used to determine the optimal design according to the scores defined in the previous section. Parameter sweeps were carried out in the FEA simulation to obtain impedance results for different values of internal radius of the secondary inductor, r_{int} as well as the distance between primary and secondary inductors, d_{inds}. The 3D model with the modifications shown in Fig. 6 was simulated in order to fine tune the system and obtain a better approximation to the experimental setup. Although the most noticeable change is the aluminum plate's shape and size, the most relevant to impedance variations are the division of the ferrite plane into annulus sectors and the discretization of the secondary inductor into evenly spaced, individual turns.

Electrical circuit simulations in the first harmonic were performed to obtain the impedance and parameters of the global system from the FEA parameter sweeps, assuming European mains voltage, 230 V, and a half-bridge inverter with symmetrical duty cycle, where the delivered power is controlled with frequency. The secondary inductor was set at 20 turns and only its capacitor was modified, C_2, as their effect

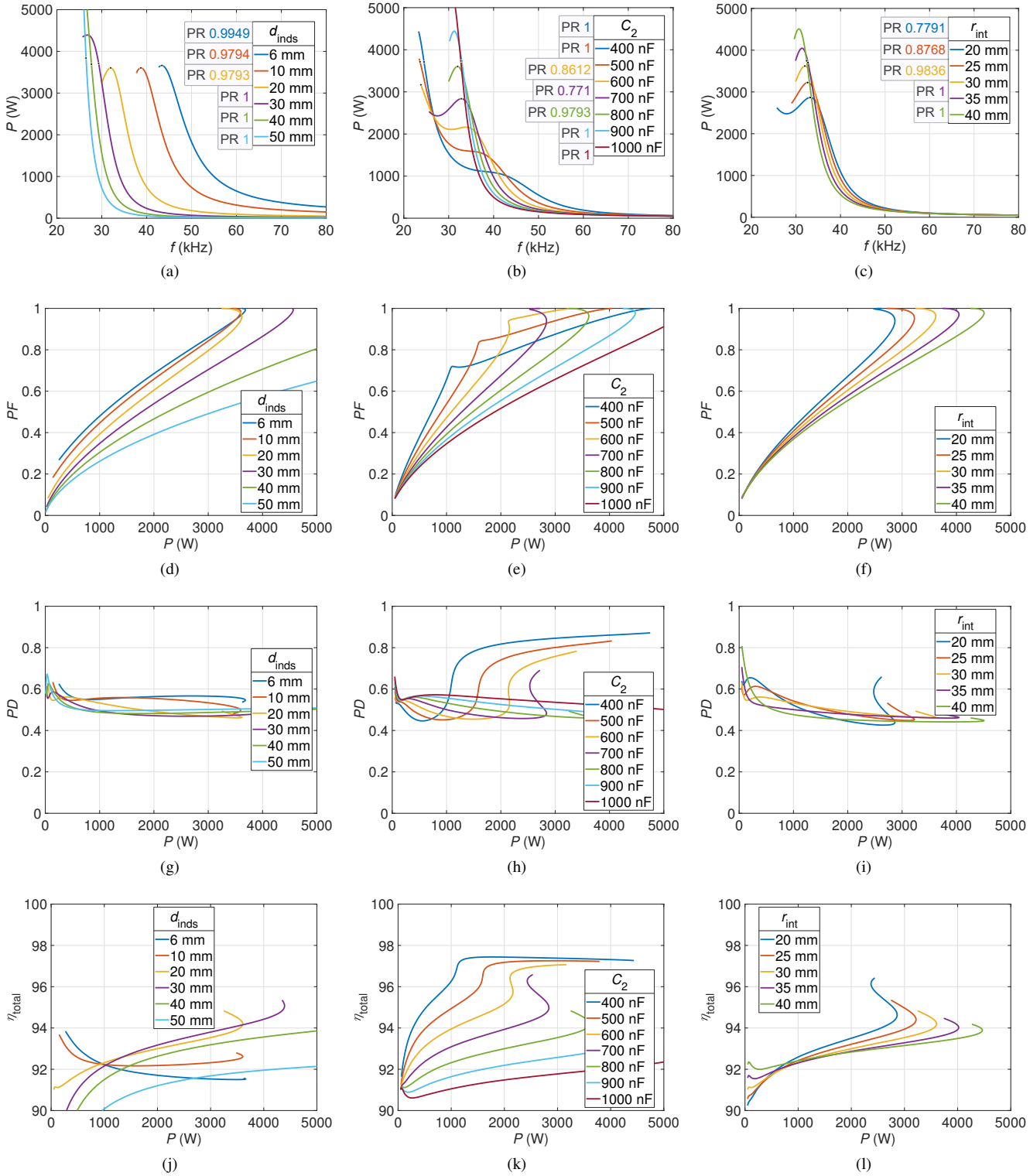

Fig. 7. Simulation results: Power delivered to the load (first row), Power Factor (second row), Power Distribution (third row), Efficiency (fourth row) considering variations of inductor to inductor distance (first column), secondary capacitor (second column) and secondary inductor internal radius (third column). The fixed values are 20 mm distance, 800 nF capacitor and 30 mm internal radius.

on global impedance can be reduced to the product $C_2 n_2^2$ [22]. The inductors' litz DC and skin wire losses were obtained analytically and their proximity losses were computed from the H field obtained in the FEA simulation and an analytical method [36], [37]. In order to reduce cost and weight of the secondary inductor, the efficiency calculations have been made assuming aluminum wire of 48 strands of 300 µm diameter.

Figure 7 shows the expected scores from the simulated cases when two of the input parameters are fixed and the other is modified. The fixed values are 20 mm for the distance between

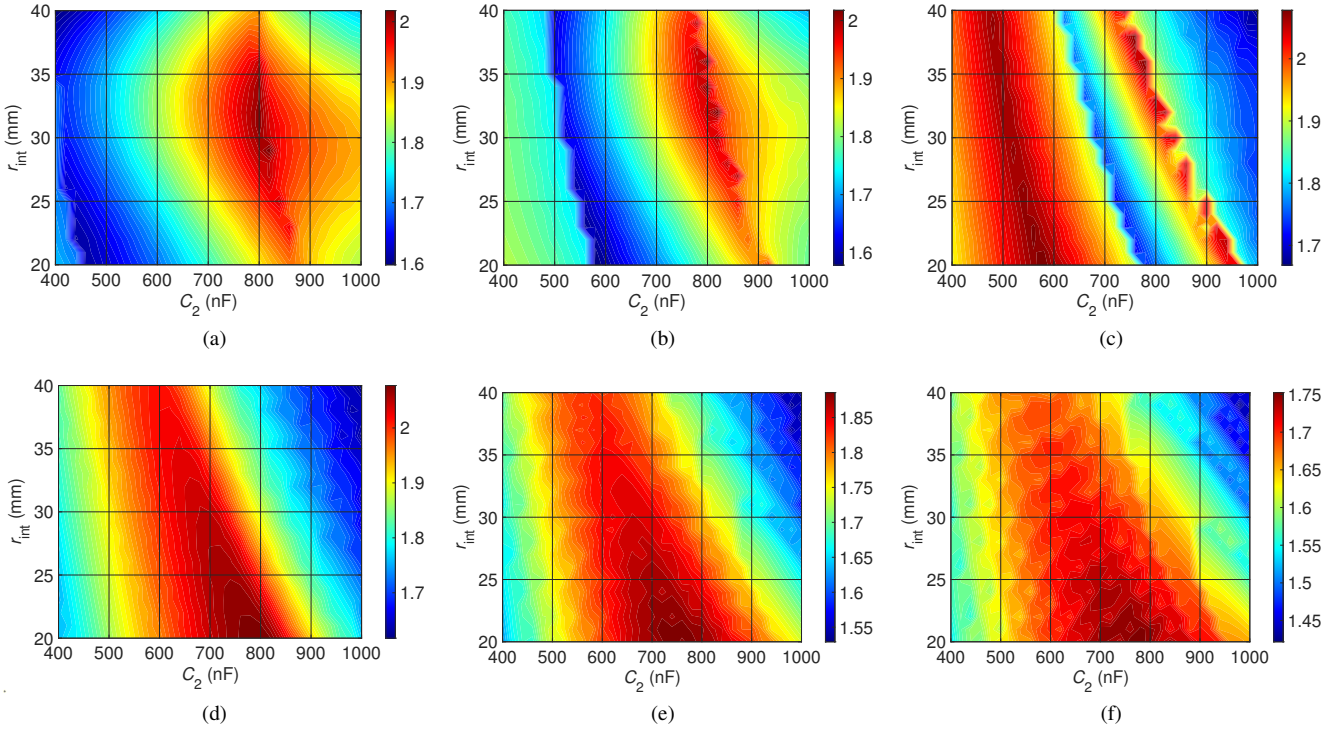

Fig. 8. Global score distribution at all simulation distances: (a) 6 mm, (b) 10 mm, (c) 20 mm, (d) 30 mm, (e) 40 mm, (f) 50 mm.

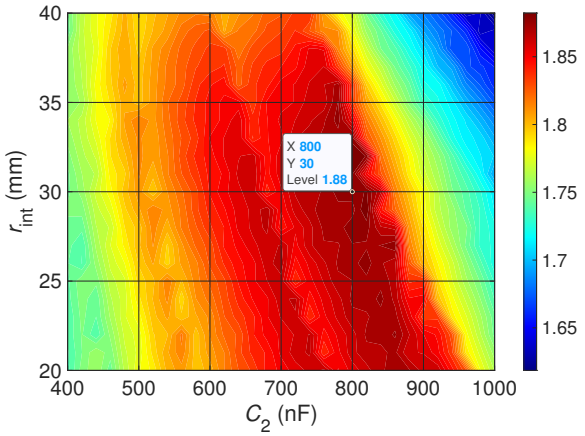

Fig. 9. Average global score distribution for all distances.

TABLE I
GLOBAL SCORE COMPARISON BETWEEN 2D AND 3D SIMULATIONS

Distance (mm)	6	10	20	30	40	50
2D GS	2.010	1.967	1.972	1.894	1.781	1.655
3D GS	2.061	2.051	2.031	1.958	1.911	1.830

primary and secondary inductors, 800 nF for the capacitor and 30 mm for the internal radius. From the second row onwards, output power is used in the horizontal axis, while the first row uses frequency. As can be appreciated, there are instances where the same values of power are reached for different frequencies due to pole splitting, so when power is used as the horizontal axis, there will be instances of the same power having different PF, PD or η_{total}, because of the different frequencies. To avoid operating in the pole splitting range, the frequency ranges to the left of the power peaks are not used.

The effects of each input parameter and frequency on each output score can be appreciated in each subfigure. In (a), PR first decreases, then increases with climbing distance. In (b), PR first decreases and then increases with bigger capacitances. In (c), PR increases with longer internal radius. In (d), PF decreases with climbing distance. In (e), PF's maximum value increases with bigger capacitances, as well as displacing said maximum to higher power points. In (f), PF's maximum is displaced to higher power points with longer internal radius. In (g), PD decreases slightly with climbing distance. In (h), PD's minimum is displaced to higher power points with bigger capacitances. In (i), PD becomes more uniform with longer internal radius. In (j), η_{total} first increases, then decreases with distance, due to the induced currents in the secondary, which has higher losses because of its aluminum wire. In (k), η_{total} decreases with C_2 increments. Finally, in (l), η_{total} decreases with r_{int} increments.

The partial incompatibility between PF and PD can be appreciated in Fig. 7, (e) and (h) for most capacitor values, where secondary resonance can be detected by a slope change in (e) and a minimum value in (h). As C_2 increases, PF increases more slowly with output power, but PD stays low for bigger power ratings. For changes in r_{int}, in Fig. 7 (c), (f), and (i), higher values allow for better PR, but PF increases more slowly, and the PD curve changes somewhat.

As can be seen from Fig. 7, PF, PD and η_{total} are frequency dependent, whereas a single score value for each simulation case would be preferable. Therefore, a weighted mean is

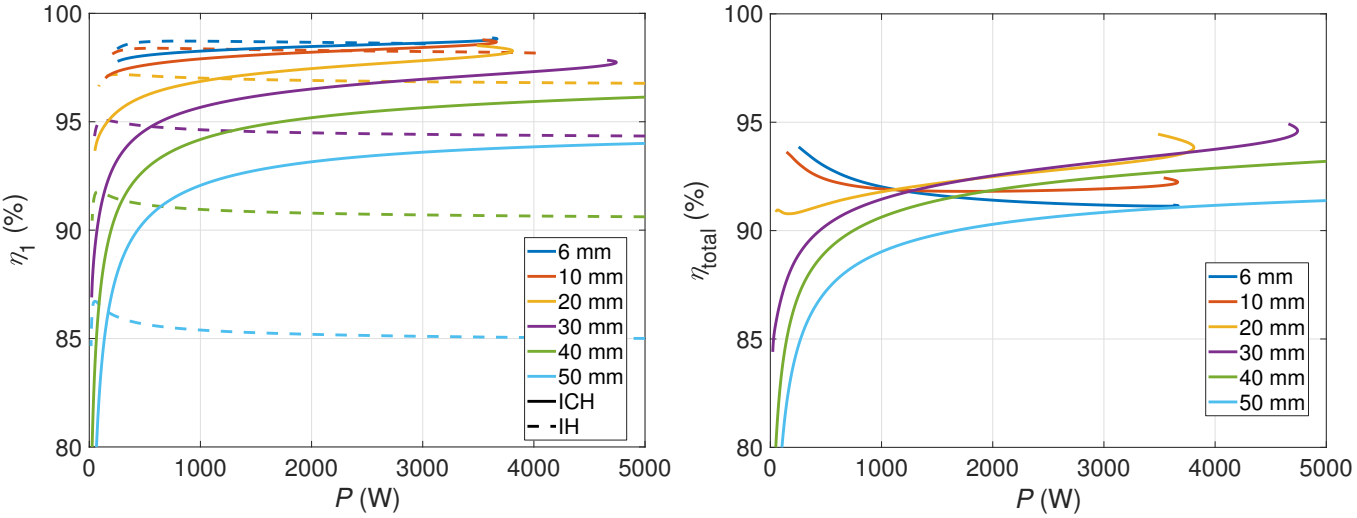

(a) (b)

Fig. 10. Simulated efficiency of (a) primary inductor in the full ICH system and heating the same load on its own, and (b) full ICH system.

calculated for each case to obtain averaged $\overline{PF}$, $\overline{PD}$ and $\overline{\eta_{\text{total}}}$ where the weights are the delivered power for each point in the figure. This way, more relevance is given to the more important high power cases, without completely ignoring low power cases.

In order to condense these results and make them more approachable, a global score, GS, is created to combine all four:

$$GS = PR + \overline{PF} - \overline{PD} + \overline{\eta_{\text{total}}}. \tag{16}$$

Weights could have been applied to prioritize scores over the others, but all are considered equally important for this optimization. Each combination of secondary capacitor and internal radius is assigned a GS value, so the optimum for each inductor to inductor distance can be easily determined from representations like Fig. 8. At smaller distances the absolute maximum is located in high values of C_2 and middle values of r_{int}, while at higher distances a new maximum appears for low C_2 and low r_{int}, moving steadily towards bigger C_2.

Finally, in order to choose the best design for all distances, GS can be averaged, as is shown on Fig. 9. The optimum design according to these criteria has an internal radius of 32 mm and uses a secondary capacitor of 800 nF, though the built prototype has 30 mm r_{int} and uses 800 nF.

IV. Viability of ICH and Comparisons with IH

A. Distance comparison with IH

As was mentioned earlier, considering the size of the secondary inductor and the simulated efficiency, instead of winding it with contiguous turns of copper wire, aluminum wire of 48 strands of 300 µm diameter was used to wind the 20 turns. The primary inductor is the same described in [22], i.e., 19 contiguous turns of copper wire of 180 strands of 200 µm diameter, the maximum number that can fit in the available space, with a ferrite plane below. The reuse of the same primary inductor for all sizes and the cable choice of the secondary inductor would help with cost reduction in commercial applications as well as their manufacturing processes.

Fig. 10 compares the efficiency of the primary inductor in a conventional IH configuration and in the ICH system, η_1, as well as the total ICH efficiency, η_{total}. The dashed line data represents simulations where the primary inductor works on its own and the full line represents the simulated data where it is part of the ICH system. The IH configuration does not use a secondary inductor, so to make the comparison fair, the inductor to load distance is considered in the IH case, while the inductor to inductor distance is considered in the ICH case, as the virtual kitchen surface thickness in both cases. η_1 is defined as:

$$\eta_1 = P_{\text{load}} / \left(P_{\text{load}} + P_{\text{sh,1}} + P_{\text{w,cond,1}} + P_{\text{w,prox,1}}\right), \tag{17}$$

where $P_{\text{sh,1}}$ are the shielding losses generated by the primary inductor, $P_{\text{w,cond,1}}$ are the conduction losses in that inductor and $P_{\text{w,prox,1}}$ are the proximity losses generated by the same inductor. This efficiency definition accounts for all losses, meaning that losses in the windings would be smaller. The figure shows that transitioning from IH to ICH, the primary inductor increases its efficiency at distances to the secondary inductor above 10 mm. Overall efficiency of the full ICH system surpasses that of the IH system after 30 mm. At first, IH efficiency is higher because having two inductors involves two sources of losses, not to mention that the overall magnetic field is increased, increasing proximity and shielding losses further. As distance increases, load resistance decreases in IH and losses increase faster, while the ICH system is able to maintain load resistances at higher distances, and losses increase more slowly. As the secondary inductor is wound with a sub-optimal aluminum wire in order to reduce cost and weight, the efficiency of the overall system catches up with the IH system at a higher distance than it would have if the secondary inductor used the same cable as the primary winding. Nevertheless, it is also important to bear in mind that

TABLE II
SCORE COMPARISON BETWEEN IH AND ICH DESIGNS

Distance (mm)		6	10	20	30	40	50
PR	IH 180	0.810	**1.000**	**1.000**	**1.000**	**1.000**	**1.000**
	IH 290	0.470	0.616	**1.000**	**1.000**	**1.000**	**1.000**
	ICH	**1.000**	**1.000**	**1.000**	**1.000**	**1.000**	**1.000**
PF	IH 180	0.706	0.621	0.408	0.283	0.212	0.170
	IH 290	**0.812**	**0.754**	**0.656**	**0.479**	**0.371**	0.306
	ICH	0.654	0.606	0.517	0.433	**0.371**	**0.313**
PD	IH 180	1.427	1.388	1.286	1.174	1.063	0.952
	IH 290	0.599	0.601	0.582	0.550	0.516	0.482
	ICH	**0.509**	**0.472**	**0.405**	**0.368**	**0.356**	**0.355**
η_{total}	IH 180	**0.987**	**0.983**	**0.970**	0.947	0.911	0.856
	IH 290	**0.987**	**0.984**	**0.972**	**0.955**	**0.931**	**0.894**
	ICH	0.919	0.922	0.922	0.912	0.897	0.872
GS	IH 180	1.075	1.215	1.088	1.004	0.994	1.050
	IH 290	1.671	1.752	**2.046**	1.884	1.774	1.719
	ICH	**2.061**	**2.051**	2.031	**1.958**	**1.911**	**1.830**

TABLE III
SCORES WHEN LOAD IS MISALIGNED AT A 20 MM DISTANCE

Misalignment (mm)		0	10	30	50	70
PR	IH 180	**1.000**	**1.000**	**1.000**	**1.000**	**1.000**
	IH 290	**1.000**	**1.000**	**1.000**	**1.000**	**1.000**
	ICH	**1.000**	**1.000**	**1.000**	**1.000**	**1.000**
PF	IH 180	0.409	0.409	0.408	0.406	0.398
	IH 290	**0.657**	**0.647**	**0.627**	**0.592**	**0.544**
	ICH	0.517	0.626	0.591	0.546	0.463
PD	IH 180	1.322	1.320	1.312	1.319	1.396
	IH 290	0.531	0.543	0.629	0.757	**0.896**
	ICH	**0.405**	**0.395**	**0.516**	**0.745**	1.066
η_{total}	IH 180	0.970	0.970	0.970	**0.970**	**0.968**
	IH 290	**0.972**	**0.972**	**0.971**	0.968	0.963
	ICH	0.922	0.928	0.939	0.951	0.959
GS	IH 180	1.054	1.056	1.064	1.056	0.971
	IH 290	**2.098**	2.075	1.969	**1.804**	**1.611**
	ICH	2.031	**2.156**	**1.996**	1.749	1.353

even in the situations where the total efficiency is lower, the losses are divided between both inductors. As shown in Fig. 10, the primary inductor of the ICH system will have less losses than the inductor in the conventional IH system.

As stated in Section III, the prototype geometry was simulated in 3D. The 3D simulation indicates that the experimental system will probably have slightly worse PF and η_{total}, but the secondary inductor turn separation provides a more uniform distribution. This is reflected in the global score comparison for all distances represented in Table I, where the beneficial effect on PD is narrowly bigger than the negative effect on PF and η_{total} on smaller distances, and more significant in higher distances. Overall, the differences are small enough to make the 2D optimum design valid for the actual 3D geometry.

To determine the differences between the ICH design and a conventional IH system, a ∅ 290 mm inductor has been designed to deliver 3680 W at a 20 mm distance between inductor and load at the same resonant frequency. For a fair comparison, the IH inductor uses the same copper cable than the primary inductor of the ICH system and the same amount of ferrite. Since the IH inductor needs 19 turns, 530 g of copper are used in the winding's construction. The primary ICH inductor uses 336 g of copper and the secondary inductor uses 101 g of aluminum. Though the IH inductor uses more material, the ICH system requires more manufacturing, making their cost roughly equivalent for this comparison.

Table II shows the scores of the primary inductor of the ICH system working on its own, the ∅ 290 mm IH inductor and the full ICH system at each simulated distance, bearing in mind that the load is slightly closer in the IH case due to the lack of a secondary inductor. Bold font is used to mark the higher scores for easier reading. For PR, in IH, R_{load} decreases with distance, preventing the design at 20 mm to deliver full power at closer distances. For PF, the IH inductor of small diameter deteriorates quickly, but the one with the biggest diameter is able to maintain better performance up to a rather high distance. For PD, the secondary inductor in the ICH system causes a lower standard deviation of the power density in the ICH case for all considered distances. For η_{total}, the large diameter of one of the IH inductors, and the use of a suboptimum material in the secondary inductor ensures a higher efficiency of the bigger IH system for all simulated distances, while the smaller IH system worsens faster. As GS is currently defined, the inability to reach full power at the lower distances due to the high R_{load}, and the overall worse distribution makes the bigger IH design slightly worse in most situations except the one it was specifically designed for.

It is relevant to consider that in IH systems of smaller diameters, such as the one shown in the Table, the penalties applied to power factor and efficiency due to the higher distance are more pronounced. ICH becomes more appealing in this situation because it overcomes the high distance problems of small and big load diameters using a single primary inductor type compatible with all secondary sizes.

Moreover, though this was not a critical concern in this comparison, reactance compensation can become a problem in IH with smaller diameters and higher distances due to the higher quality factor of the equivalent impedance. In order to deliver the same amount of power and thus achieve the same equivalent load resistance, the ICH system entails a much lower equivalent inductance than that of an IH system. In the 20 mm case of the comparison, the ICH system has a L_{eq} of 35 µH and the ∅ 290 mm IH system has 52.5 µH at 30 kHz. This results on a RMS capacitor voltage of 220 V in the ICH system and 300 V in the IH system at 3000 W, despite the better PF in the IH system.

B. Lateral misalignment

The effects of lateral misalignment are very important in WPT applications, particularly when precise positioning is not achievable, such as in electric vehicle charging [17], [18]. In the case of the proposed ICH system, significant misalignments should be easily detected and corrected by attentive users, but their effects must still be determined in order to know whether preventive or corrective actions are needed. Therefore, simulations at a 20 mm distance have been carried out, where the load and its attached secondary

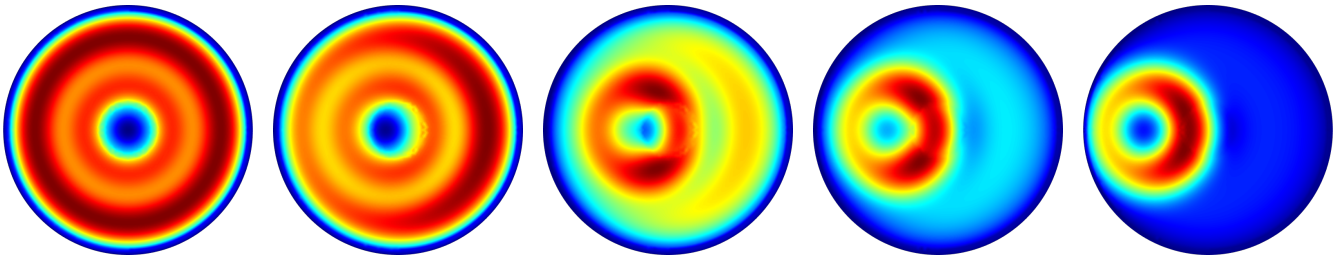

(a) (b) (c) (d) (e)

Fig. 11. Power distribution of load misalignment at 20 mm distance and 3680 W: (a) 0 mm, (b) 10 mm, (c) 30 mm, (d) 50 mm, (e) 70 mm.

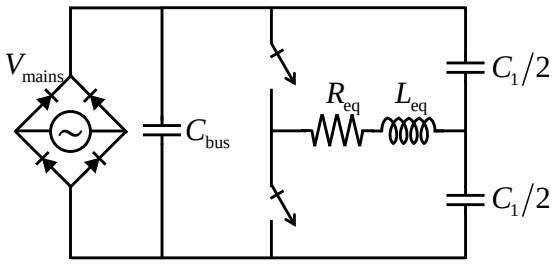

Fig. 12. Setup topology.

inductor are misaligned up to 70 mm, almost half their radius. Additionally, lateral misalignments with only the ∅ 180 mm primary inductor and the ∅ 290 mm IH inductor described in the previous section have also been simulated for further comparison.

Table III shows the score results for all three simulations. In both IH simulations, all parameters except PR slowly and steadily worsen with misalignment. In the particular case of the ∅ 180 mm inductor, the variations are very small because the ∅ 290 mm load never stops covering the inductor. In the ICH case, PR is not affected, PF first increases and then decreases, PD worsens significantly, and η_{total} improves slightly. As the inductors are misaligned, coupling is reduced and the secondary inductor receives less and less power, worsening distribution and reducing secondary losses. At first, the coupling reduction also results in better impedance matching for this distance, but PF eventually worsens as well. Overall, the system can function with the simulated misalignments without adverse effects to the electronics, but the heating performance is strongly penalized. In comparison, the ICH system is slightly better for small misalignments and the ∅ 290 mm IH system is narrowly more robust to high misalignments.

The simulated distributions at maximum power are shown in Fig. 11. Although the most problematic misalignments should be easy to spot for most people, the ICH system would probably benefit from a guiding system of some kind, which at least should able to detect whether the load is centered or not.

V. Experimental Results

The system is fed with the half-bridge inverter shown in Fig. 12 with symmetrical duty cycle, using only the frequency to control power. Voltage and current probes have been used to measure inverter voltage, primary inductor current and voltage and secondary inductor current and voltage. Sample captures are shown on Figs. 13 and 14, where C1 is the inverter output voltage, V_0, C2 is the primary inductor voltage, V_{l1}, C3 is the secondary inductor voltage, V_{l2}, C4 is the primary current, I_1, and C5 is the secondary current, I_2.

The experimental setup is shown in Fig. 15. The experimental ICH system is on the left of the Figure, as close as possible to the 3D simulated geometry, using PPS (polyphenylene sulfide) separators between inductors to achieve the simulated distances. On the right, the oscilloscope employed is shown. The electronics converter was repurposed from a commercially available IH appliance.

Despite ICH and WPT being similar systems, induction heating efficiency can not be measured directly. Since load resistances are part of the equivalent series resistance (5), (8), and there are no effective ways to measure induced voltage and currents in the ferromagnetic load, there is no accesible terminal to measure load power [5].

In order to evidence the improvement from a single inductor to the full ICH system and verify the impedance matrix, measurements with the secondary in open circuit were first taken for the smaller distances, as shown on Fig. 16. The measured inductance values on Fig. 16 (d) and (f) at low frequencies peel away from the simulated predictions. The most likely causes are the geometric tolerances and the saturation of the vessel material at high magnetic field strength, both of which explain why the effect is lessened at farther distances between inductors.

Further measurements of the full system were taken for most simulated distances, whose results are shown on Fig. 17. The experimental measurements confirm the simulated results in most cases, and the comparison with the open secondary results shows the significant improvement in PF and primary current from the ∅ 180 mm IH system to the full ICH system. As can be seen in Fig. 17 (a), there is discrepancy in the power versus frequency measurement for the smaller distances. As confirmed by Fig. 17 (f), the inductance errors from the impedance matrix directly affect L_{eq}.

In order to qualitatively determine the uniformity of the power distribution, pictures were taken boiling water at a 10 mm distance between inductors and 3000 W of power, shown on Fig. 18. Additionally, thermographic images without water were taken for more quantitative results, shown on Fig.

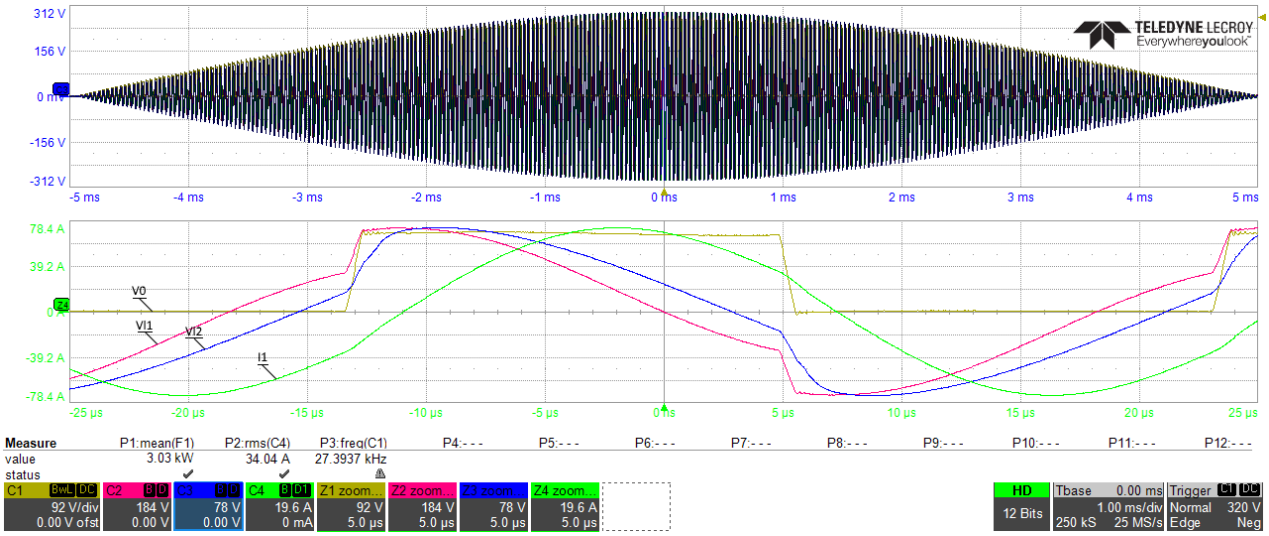

Fig. 13. Oscilloscope capture of the system with the secondary in open circuit at 10 mm delivering 3000 W.

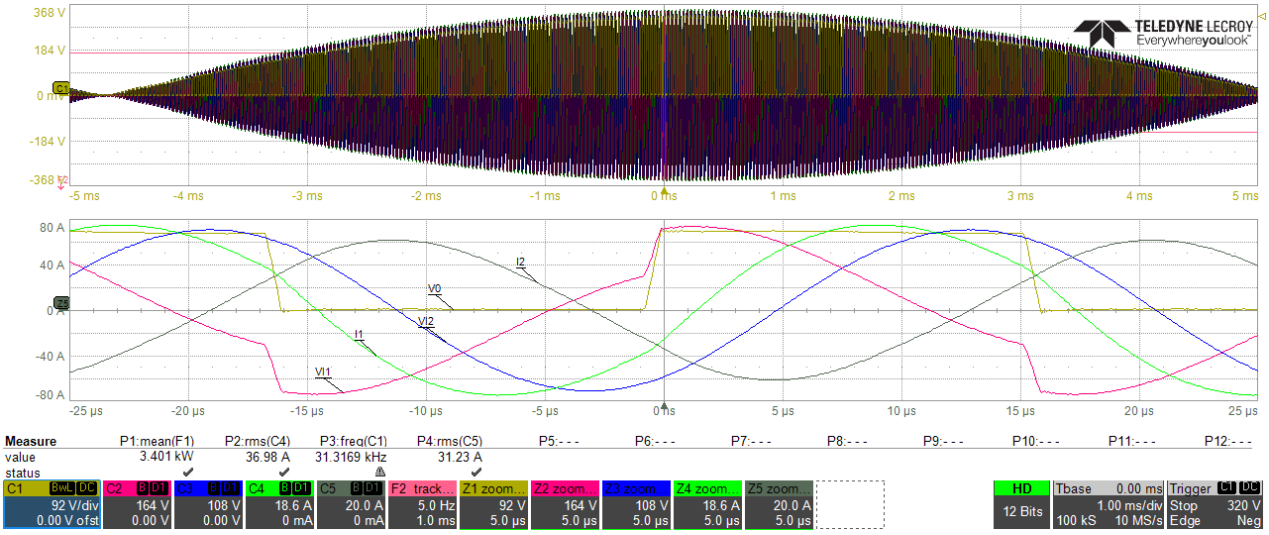

Fig. 14. Oscilloscope capture of the full system at 20 mm delivering 3400 W.

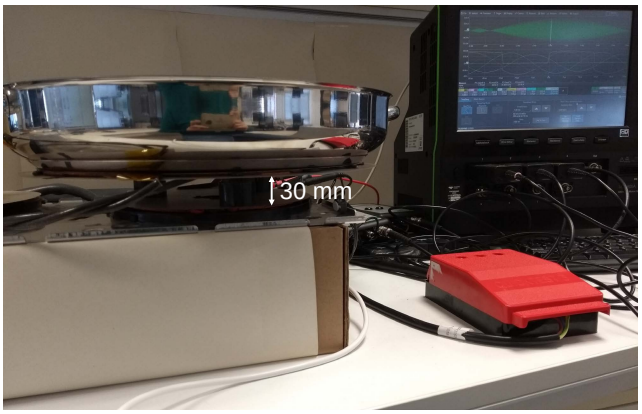

Fig. 15. Experimental setup.

19. These images were taken when a sudden power of 3000 W was applied to the room temperature vessel. The intent was to obtain a temperature distribution as close as possible to the power distribution by minimizing the time in which the heat transfer mechanisms could act. Mean temperature and standard deviation on the vessel's surface are 28.8 °C and 6.3 °C respectively in Fig 19 (a) and 37.8 °C and 2.7 °C in Fig 19 (b). Both figures confirm that the system design provides good power distribution, as expected from the simulations.

VI. Conclusion

The simulations and experimental results demonstrate that inductively coupled heating can indeed be used to adapt a relatively big vessel to a small primary inductor, highlighting the improvement of the ICH system over the traditional IH system. The defined scores allowed an easier optimization complying with the design goals of power delivery, power distribution, electronics stress and efficiency. The simulations were verified with experimental results in terms of system

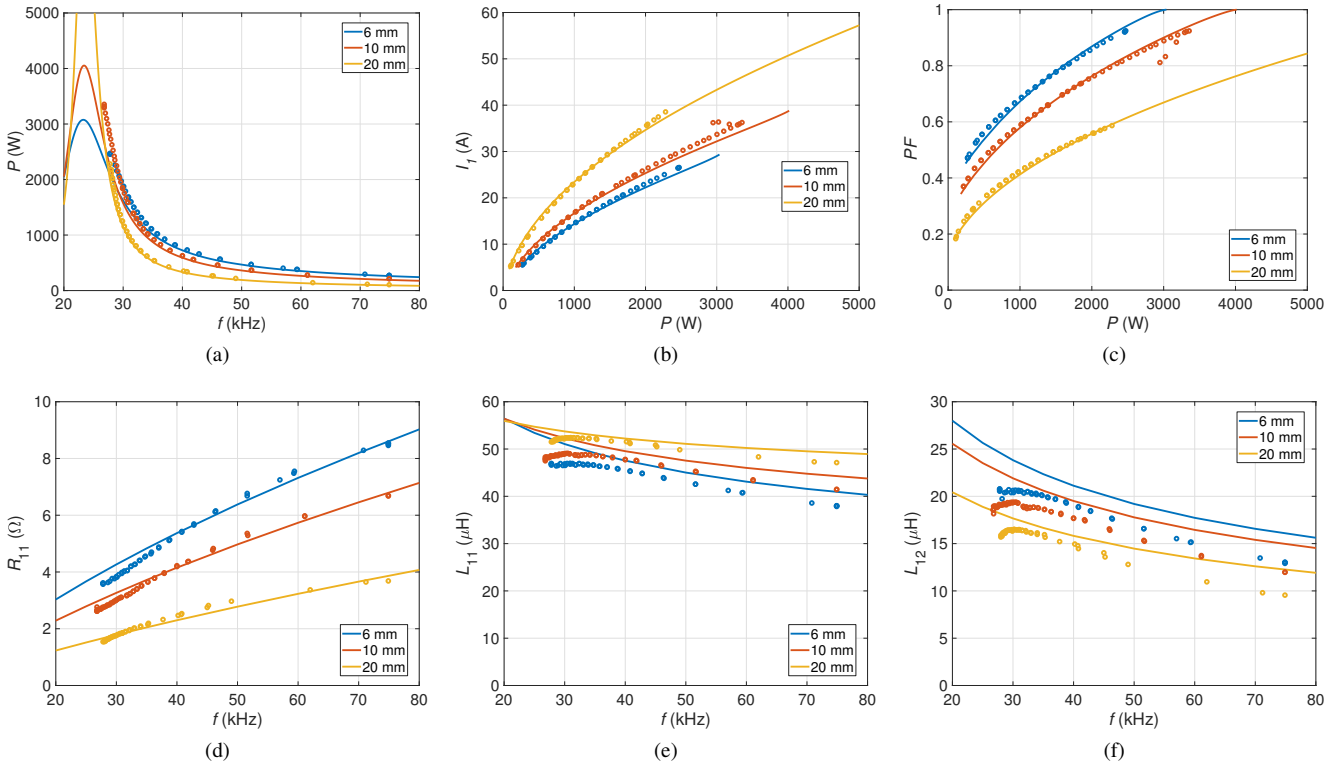

Fig. 16. Open secondary experimental results.

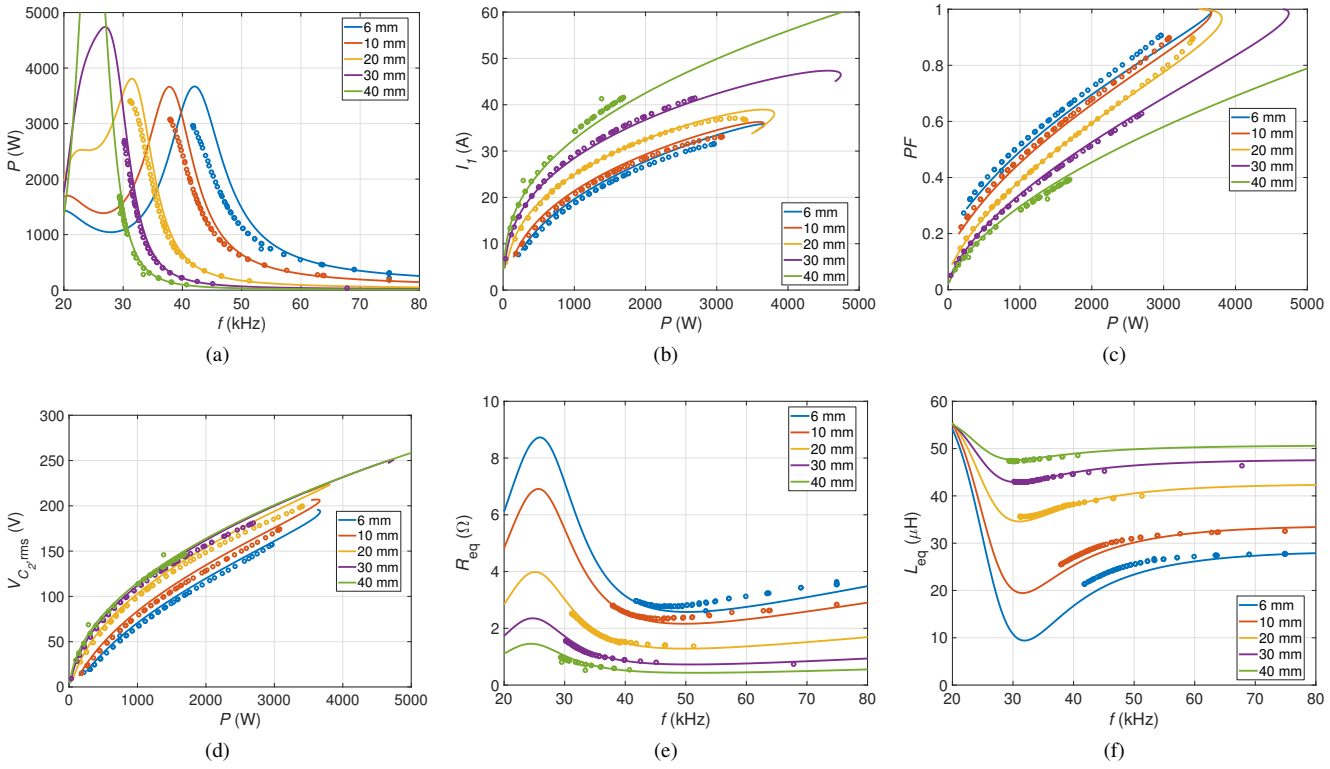

Fig. 17. ICH system experimental results.

impedance and electric parameters, as well as the power distribution.

The results prove that ICH can be used effectively at distances higher than 10 mm while achieving the design goals. Therefore, it is suitable to implement the seamless induction concept without the disadvantages of losing kitchen surface

(a) (b)

Fig. 18. Water boiling at high power with secondary inductor (a) off and (b) on.

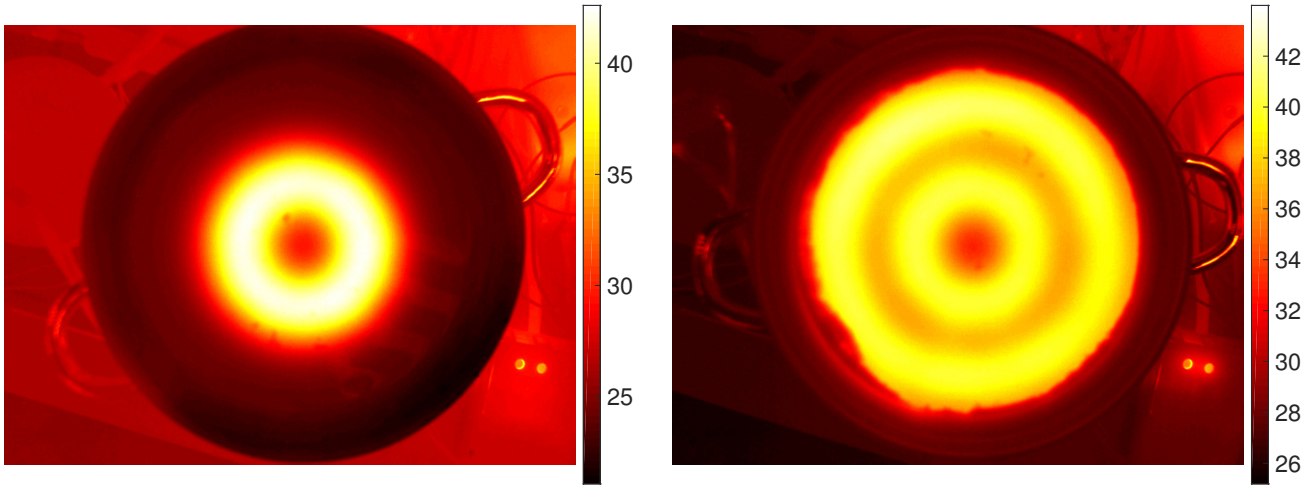

(a) (b)

Fig. 19. Thermographic images with (a) only the primary inductor and (b) the full system.

thickness or the disadvantages of increased distance in conventional IH applications. The use of the most common inverter and control methods also ensures a smoother transition from a conventional IH appliance to an ICH appliance.

Lateral misalignment does not negatively affect the electronics, but it penalizes power distribution significantly. Guiding systems should be explored to implement the system into a finished, commercial product. The guidance could rely on mutual impedance measurements, voltage measurements in an array of small inductors, or similar techniques.

Analogous design processes can be carried out to adapt vessel sizes from 90 to 300 mm to the same primary inductor, eventually allowing to create appliances with these identical primary inductors in any fixed configuration and all compatible secondary-vessel combinations could function on top of any of them.

Although the prototype is not optimal for each individual goal and inductor distance, it is the most versatile for the distance range presented. On the one hand, if the final application had a fixed distance, the design could be optimized for that situation only. On the other hand, if optimum performance was desired in all cases, a further improvement of the design could be the ability for the secondary capacitor to switch values to best suit each situation.

REFERENCES

[1] J. Acero, J. M. Burdio, L. A. Barragan, D. Navarro, R. Alonso, J. Ramon, F. Monterde, P. Hernandez, S. Llorente, and I. Garde, "Domestic induction appliances," *IEEE Industry Applications Magazine*, vol. 16, no. 2, pp. 39–47, Mar. 2010.

[2] O. Lucía, P. Maussion, E. J. Dede, and J. M. Burdío, "Induction heating technology and its applications: Past developments, current technology, and future challenges," *IEEE Transactions on Industrial Electronics*, vol. 61, no. 5, pp. 2509–2520, May 2014.

[3] J. Villa, J. I. Artigas, J. R. Beltrán, A. D. Vicente, and L. A. Barragán, "Analysis of the acoustic noise spectrum of domestic induction heating systems controlled by phase-accumulator modulators," *IEEE Transactions on Industrial Electronics*, vol. 66, no. 8, pp. 5929–5938, Aug. 2019.

[4] I. Lope, J. Acero, and C. Carretero, "Analysis and optimization of the efficiency of induction heating applications with litz-wire planar and solenoidal coils," *IEEE Transactions on Power Electronics*, vol. 31, no. 7, pp. 5089–5101, Jul. 2016.

[5] J. Acero, C. Carretero, I. Millán, R. Alonso, O. Lucía, and J. M. Burdío, "Experimental setup for inductive efficiency measurements of domestic induction systems based on energy balance," in *IECON 2010 - 36th Annual Conference on IEEE Industrial Electronics Society*, 2010, pp. 114–119.

[6] V. Esteve, J. Jordán, E. Sanchis-Kilders, E. J. Dede, E. Maset, J. B. Ejea, and A. Ferreres, "Enhanced pulse-density-modulated power control for high-frequency induction heating inverters," *IEEE Trans. Ind. Electron.*, vol. 62, no. 11, pp. 6905–6914, Nov. 2015.

[7] L. Meng, K. W. E. Cheng, and K. W. Chan, "Systematic approach to high-power and energy-efficient industrial induction cooker system: Circuit design, control strategy, and prototype evaluation," vol. 26, pp. 3754–3765, 2011.

[8] H. N. Pham, H. Fujita, K. Ozaki, and N. Uchida, "Estimating method of heat distribution using 3-d resistance matrix for zone-control induction heating systems," vol. 27, pp. 3374–3382, 2012.

[9] T. Mishima, C. Takami, and M. Nakaoka, "A new current phasor-controlled ZVS twin half-bridge high-frequency resonant inverter for induction heating," *IEEE Trans. Ind. Electron.*, vol. 61, no. 5, pp. 2531–2545, May 2014.

[10] T. Mishima and M. Nakaoka, "A load-power adaptive dual pulse modulated current phasor-controlled zvs high-frequency resonant inverter for induction heating applications," vol. 29, pp. 3864–3880, 2014.

[11] C. Carretero, J. Acero, R. Alonso, and J. M. Burdio, "Normal-mode decomposition of surface power distribution in multiple-coil induction heating systems," *IEEE Transactions on Magnetics*, vol. 52, no. 2, pp. 1–8, 2016.

[12] E. Plumed, J. Acero, I. Lope, and J. M. Burdío, "Design methodology of high performance domestic induction heating systems under worktop," *IET Power Electronics*, oct 2019.

[13] G. A. Covic and J. T. Boys, "Inductive power transfer," *Proc. IEEE*, vol. 101, no. 6, pp. 1276–1289, Jun. 2013.

[14] J. Garnica, R. A. Chinga, and J. Lin, "Wireless power transmission: From far field to near field," *Proceedings of the IEEE*, vol. 101, no. 6, pp. 1321–1331, Jun. 2013.

[15] T. Kan, T.-D. Nguyen, J. C. White, R. K. Malhan, and C. C. Mi, "A new integration method for an electric vehicle wireless charging system using lcc compensation topology: Analysis and design," vol. 32, pp. 1638–1650, 2017.

[16] J. Huang, Y. Zhou, Z. Ning, and H. Gharavi, "Wireless power transfer and energy harvesting: Current status and future prospects," *IEEE Wireless Communications*, vol. 26, no. 4, pp. 163–169, Aug. 2019.

[17] F. J. López-Alcolea, J. V. d. Real, P. Roncero-Sánchez, and A. P. Torres, "Modeling of a magnetic coupler based on single- and double-layered rectangular planar coils with in-plane misalignment for wireless power transfer," *IEEE Transactions on Power Electronics*, vol. 35, no. 5, pp. 5102–5121, 2020.

[18] N. Khan, H. Matsumoto, and O. Trescases, "Wireless electric vehicle charger with electromagnetic coil-based position correction using impedance and resonant frequency detection," *IEEE Transactions on Power Electronics*, vol. 35, no. 8, pp. 7873–7883, 2020.

[19] W. Han, K. T. Chau, and Z. Zhang, "Flexible induction heating using magnetic resonant coupling," *IEEE Transactions on Industrial Electronics*, vol. 64, no. 3, pp. 1982–1992, Mar. 2017.

[20] W. Han, K. T. Chau, Z. Zhang, and C. Jiang, "Single-source multiple-coil homogeneous induction heating," *IEEE Transactions on Magnetics*, vol. 53, no. 11, pp. 1–6, Nov. 2017.

[21] W. Han, K. T. Chau, C. Jiang, and W. Liu, "All-metal domestic induction heating using single-frequency double-layer coils," *IEEE Transactions on Magnetics*, vol. 54, no. 11, pp. 1–5, Nov. 2018.

[22] E. Plumed, I. Lope, J. Acero, and J. M. Burdio, "Inductor system evaluation for simultaneous wireless energy transfer and induction heating," in *Proc. IECON 2018 - 44th Annual Conf. of the IEEE Industrial Electronics Society*, Oct. 2018, pp. 3509–3514.

[23] E. Plumed, I. Lope, J. Acero, and J. M. Burdío, "Design of a three inductor system with one externally fed for an inductively coupled heating application," in *Proc. IECON 2019 - 45th Annual Conf. of the IEEE Industrial Electronics Society*, vol. 1, Oct. 2019, pp. 5070–5074.

[24] R. C. M. Gomes, M. A. Vitorino, D. A. Acevedo-Bueno, and M. B. de Rossiter Corrêa, "Multiphase resonant inverter with coupled coils for ac-ac induction heating application," vol. 56, pp. 551–560, 2020.

[25] O. Lucia, J. Acero, C. Carretero, and J. M. Burdio, "Induction heating appliances: Toward more flexible cooking surfaces," *IEEE Industrial Electronics Magazine*, vol. 7, no. 3, pp. 35–47, Sep. 2013.

[26] L. C. Meng, K. W. E. Cheng, and S. L. Ho, "Multicoils design for induction cookers with applying switched exciting method," vol. 48, pp. 4503–4506, 2012.

[27] J. Acero, C. Carretero, . Lucía, R. Alonso, and J. M. Burdío, "Mutual impedance of small ring-type coils for multiwinding induction heating appliances," *IEEE Transactions on Power Electronics*, vol. 28, no. 2, pp. 1025–1035, Feb. 2013.

[28] H. Sarnago, J. M. Burdío, and . Lucía, "High-performance and cost-effective ZCS matrix resonant inverter for total active surface induction heating appliances," *IEEE Transactions on Power Electronics*, vol. 34, no. 1, pp. 117–125, Jan. 2019.

[29] J. Serrano, I. Lope, and J. Acero, "Nonplanar overlapped inductors applied to domestic induction heating appliances," *IEEE Transactions on Industrial Electronics*, vol. 66, no. 9, pp. 6916–6924, Sep. 2019.

[30] F. Sanz, C. Sagues, and S. Llorente, "Induction heating appliance with a mobile double-coil inductor," *IEEE Transactions on Industry Applications*, vol. 51, no. 3, pp. 1945–1952, May 2015.

[31] J. M. Palacios-Gasós, E. Montijano, C. Sagüés, and S. Llorente, "Cooperative periodic coverage with collision avoidance," *IEEE Transactions on Control Systems Technology*, vol. 27, no. 4, pp. 1411–1422, Jul. 2019.

[32] K. Song, Z. Li, J. Jiang, and C. Zhu, "Constant current/voltage charging operation for series–series and series–parallel compensated wireless power transfer systems employing primary-side controller," *IEEE Transactions on Power Electronics*, vol. 33, no. 9, pp. 8065–8080, Sep. 2018.

[33] J. Yin, D. Lin, T. Parisini, and S. Y. Hui, "Front-end monitoring of the mutual inductance and load resistance in a series–series compensated wireless power transfer system," *IEEE Transactions on Power Electronics*, vol. 31, no. 10, pp. 7339–7352, Oct. 2016.

[34] J. Hou, Q. Chen, Z. Zhang, S. Wong, and C. K. Tse, "Analysis of output current characteristics for higher order primary compensation in inductive power transfer systems," *IEEE Transactions on Power Electronics*, vol. 33, no. 8, pp. 6807–6821, Aug. 2018.

[35] U. Iruretagoyena, A. Garcia-Bediaga, L. Mir, H. Camblong, and I. Villar, "Bifurcation limits and non-idealities effects in a three-phase dynamic ipt system," *IEEE Transactions on Power Electronics*, vol. 35, no. 1, pp. 208–219, Jan. 2020.

[36] C. Carretero, "Coupling power losses in inductive power transfer systems with litz-wire coils," *IEEE Trans. Ind. Electron.*, vol. 64, no. 6, pp. 4474–4482, Jun. 2017.

[37] Q. Deng, J. Liu, D. Czarkowski, M. K. Kazimierczuk, M. Bojarski, H. Zhou, and W. Hu, "Frequency-dependent resistance of litz-wire square solenoid coils and quality factor optimization for wireless power transfer," *IEEE Transactions on Industrial Electronics*, vol. 63, no. 5, pp. 2825–2837, May 2016.

Emilio Plumed (S'17) received the M.Sc. in industrial engineering from the Universidad de Zaragoza, Zaragoza, Spain in 2016. From then on, he has been with the Department of Electronic Engineering and Communications at the Universidad de Zaragoza, Spain, working on obtaining his Ph.D. degree in electronic engineering. His research interests include electromagnetic modelling of induction heating (IH) systems and hybrid IH and wireless power transfer systems.

Ignacio Lope (M'16) received the M.Sc. degree in electrical engineering and the Ph.D. degree in power electronics from the Universidad de Zaragoza, Zaragoza, Spain, in 2010 and 2015, respectively. He is currently with the BSH Home Appliances, Zaragoza, where he is involved in several projects focusing on developing domestic induction heating appliances. Currently, he is also an Adjunct Professor with the Department of Applied Physics at the Universidad de Zaragoza, Spain. His current research interests include electromagnetic modeling of inductive coupled contactless energy transfer systems and loss modeling of magnetic devices.

Jesús Acero (M'06, SM'20) received the M.Sc. and Ph.D. degrees in electrical engineering from the Universidad de Zaragoza, Zaragoza, Spain, in 1992 and 2005, respectively. From 1992 to 2000, he worked in several industry projects, especially focused on custom power supplies for research laboratories. From 2000 he has been with the Department of Electronic Engineering and Communications at the Universidad de Zaragoza, Spain, where he is currently a Professor. His main research interests include resonant converters for induction heating applications, inductive-type load modeling, and electromagnetic modeling. Dr. Acero a Member of the IEEE Power Electronics, Industrial Electronics and Magnetics Societies. He is also a member of the Instituto de Investigación en Ingeniería de Aragón (I3A).